ARTICLE

Ag-Ru interface for highly efficient hydrazine assisted water electrolysis

Received 00th January 20xx,
Accepted 00th January 20xx

DOI: 10.1039/x0xx00000x

Xiaoyang Fu,[a] Dongfang Cheng,[b] Ao Zhang,[c] Jingxuan Zhou,[a] Sibo Wang,[a] Xun Zhao,[d] Jun Chen,[d] Philippe Sautet,*[ab], Yu Huang*[c] and Xiangfeng Duan*[a]

Hydrazine assisted water electrolysis offers an attractive pathway for low-voltage hydrogen production while at the same time mitigating the hazardous hydrazine environmental pollutants. Herein we report the design and synthesis of Ru decorated Ag nanoparticles (NPs) where the Ag-Ru interfaces act as highly effective bifunctional electrocatalysts for the hydrazine oxidation reaction (HzOR) and the hydrogen evolution reaction (HER). The electrocatalysts with Ag-Ru interfaces demonstrate improved HzOR performance with lower overpotential, enhanced mass activity (MA) and highly selective oxidation of hydrazine into N_2. Density function theory (DFT) computations reveal the Ag-Ru interfaces feature higher barrier for N-N bond cleavage and easier N_2 desorption, contributing to the electrocatalytic activity and selectivity. At the same time, improved HER performance is also observed due to the more favorable hydrogen desorption. Together, by employing the Ru decorated Ag NPs as electrocatalysts for both HzOR and HER, the hydrazine assisted water electrolyser delivers record-high performance with a current density of 100 mA/cm^2 at an ultralow cell voltage of 16 mV and a high current density of 983±30 mA/cm^2 at a cell voltage of 0.45 V without any IR compensation.

Introduction

Hydrazine assisted water electrolysis can greatly lower the required voltage and energy consumption for green hydrogen production by replacing the sluggish oxygen evolution reaction (OER, E^0=1.23V) in conventional water electrolysis with the hydrazine oxidation reaction (HzOR, E^0=-0.33V, Eq.1)[1]. At the same time, this process also helps remove hazardous and carcinogenic hydrazine from industrial wastewater[2-5], for example, the hydrazine concentration of the wastewater surrogate for the chemical decontamination of nuclear facilities may reach up to 0.1 mol/L (ref.[6]). Apart from the advantages of saving energy and removing hazards, the degradation of the electrolyser system[7-9] (e.g., binder, anion exchange membrane (AEM) and electrocatalysts) can also be alleviated at much lower cell voltage and temperature. In addition, the production of hydrogen and nitrogen gas is also comparably safer than the concurrent production of hydrogen and oxygen in the conventional water electrolysers upon crossover[10, 11].

Ru based electrocatalysts have been reported to be highly effective for HzOR with the lowest overpotential for hydrazine electrooxidation[12]. However, at the same time, both theoretical and experimental studies also suggest that Ru surface may facilitate the undesirable cleavage of the N-N bonds[13, 14], leading to incomplete oxidation of hydrazine with ammonia as a potential by-product (Eq.2)[12, 15, 16], which is not only hazardous but also lowers its utilization efficiency. Previous theoretical studies suggest that Ag could significantly increase the free energy barrier for the N-N bond cleavage[13, 14], which could prevent ammonia by-product formation. However, Ag is also unfavourable for the N-H bond cleavage[13, 14], thus making it unsuitable for electrocatalytic HzOR. Indeed, previous experimental study have also shown that Ag exhibited a very high overpotential for HzOR despite of its capability in achieving selective electrooxidation into N_2 [12].

$$N_2H_4 + 4OH^- \rightarrow N_2 + 4H_2O + 4e^- \quad (1)$$

$$N_2H_4 + OH^- \rightarrow 1/2N_2 + NH_3 + H_2O + e^- \quad (2)$$

In addition, for the HER on the cathode side, Ru-based electrocatalysts have also been widely studied in alkaline media since they provide the desired oxophilicity to facilitate the water dissociation step[17-19]. However, according to the HER activity volcano plot, Ru suffers from too strong binding with H, which limits the HER performance[20, 21]. In this regard, Ag may also lower the metal-hydrogen binding energy and improve HER performance. For example, the RuAu single atom alloy has been studied as a good HER electrocatalysts, due to the lower H binding energy with Au[22]. Thus, as an analogy, Ag may play a similar role in weakening the M-H binding energy and serve as a cheaper alternative to Au to facilitate HER.

Herein, we report the design and synthesis of bimetallic Ru decorated Ag nanoparticles (Ru@Ag NPs) as bifunctional

[a] Department of Chemistry and Biochemistry, University of California, Los Angeles, Los Angeles, CA 90095, USA. Email: xduan@chem.ucla.edu
[b] Department of Chemical and Biomolecular Engineering, University of California, Los Angeles, Los Angeles, CA 90095, USA. Email: sautet@ucla.edu
[c] Department of Materials Science and Engineering, University of California, Los Angeles, Los Angeles, CA 90095, USA. Email: yhuang@seas.ucla.edu
[d] Department of Bioengineering, University of California, Los Angeles, Los Angeles, CA 90095, USA.

†Electronic Supplementary Information (ESI) available: [details of any supplementary information available should be included here]. See DOI: 10.1039/x0xx00000x

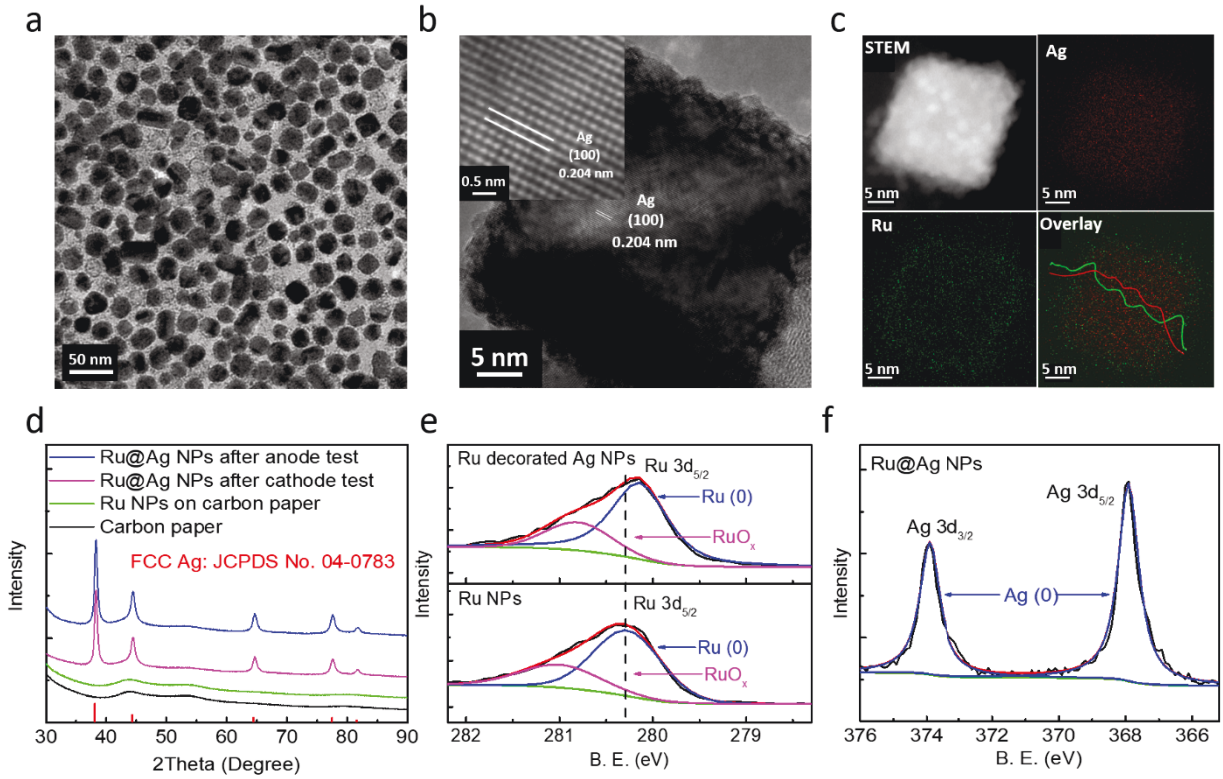

Fig. 1 (a) TEM image of Ru@Ag NPs. (b) HRTEM image of Ru@Ag NPs. (c) STEM and EDX characterizations of Ru@Ag NPs with the line-scans for Ru (green line) and Ag (red line) shown in the lower-right panel. (d) XRD characterization of Ru@Ag NPs under working conditions, small Ru NPs and carbon paper. (e) XPS spectra of Ru for Ru@Ag NPs and small Ru NPs. (f) XPS spectra of Ag for Ru@Ag NPs.

electrocatalysts for both HzOR and HER. We show that the Ru@Ag NPs effectively inhibit N-N bond cleavage while lowering the HzOR overpotential. Rotating disk electrode (RDE) tests reveal an electron transfer number of four, confirming the complete oxidation of hydrazine to environmentally friendly nitrogen gas. The Ru@Ag catalysts exhibited 1.3-fold higher mass activity (MA) for HzOR and 3.6 times improvement in HER performances than ultrasmall Ru NPs. By employing the Ru@Ag NPs for both the anode HzOR and cathode HER via a membrane electrode assembly (MEA) process, the hydrazine assisted water electrolyser delivers record-high performance, with a current density of 100 mA/cm^2 at an ultralow cell voltage of 16 mV and ultrahigh current density of 983±30 mA/cm^2 at the cell voltage of 0.45 V under room temperature without any IR compensation. Chronopotentiometry (CP) tests further demonstrate robust long-term performance over 110-hour period.

Results and discussion

Synthesis and characterization

The Ru@Ag NPs were prepared through a one-pot polyol synthesis with $AgNO_3$ and $RuCl_3$ as the precursors, ethylene glycol as the solvent and reducing agent, and polyvinylpyrrolidone (PVP) as the template agent, respectively. Transmission electron microscope (TEM) images (Fig. 1a) reveals the as-prepared electrocatalysts consist of Ag NPs (27.1 ± 4.3 nm, Fig. S1a, ESI†) decorated with ultrasmall Ru NPs (2.50 ± 0.34 nm, Fig. S1b, ESI†). The high resolution TEM (HRTEM) further confirms the lattice spacing of 0.203 nm for the Ag (100) lattice planes (Fig. 1b)[23]. As a control sample, the ultrasmall Ru NPs (2.47 ± 0.35 nm) were also synthesized under the similar condition without the addition of $AgNO_3$ (Fig. S2, ESI†). Scanning transmission electron microscope (STEM) and corresponding energy dispersive X-ray spectroscopy (EDX) mapping images of the Ru@Ag NPs also demonstrate a relative uniform distribution of Ag and Ru elements in the resulting NPs (Fig. 1c). X-Ray diffraction (XRD) shows the characteristic peaks for face centred cubic (FCC) Ag in the electrocatalysts under working conditions without any peaks corresponding to alloy phase formation between Ag and Ru (Fig. 1d). No peaks corresponding to Ru can be observed in the samples of ultrasmall Ru NPs and Ru@Ag NPs, indicating the ultrasmall Ru NPs are amorphous, consistent with the previous studies[24]. Elemental analysis using the inductively coupled plasma atomic emission spectroscopy (ICP-AES) indicates the overall atomic ratio (Ru:Ag=0.5 ± 0.05:1) is in agreement with the feed ratio during the synthesis. The X-ray photoelectron spectroscopy (XPS) study showed the characteristic peaks for Ru 3d (Fig. 1e) and Ag 3d (Fig. 1f) with a surficial elemental ratio (Ru:Ag) of 1.00:1.08. The higher surficial Ru content also agrees with the ultrasmall Ru NPs decoration on the Ag NPs surface. Importantly, the Ru 3d peak for Ru@Ag NPs shifts to lower binding energy by 0.2 eV compared with that of the Ru NPs (Fig. 1e), indicating a slight charge transfer from Ag to Ru, likely due to their electronegativity difference) (electronegativity: 1.93 for Ag and 2.2 for Ru).

Electrochemical study on single electrode

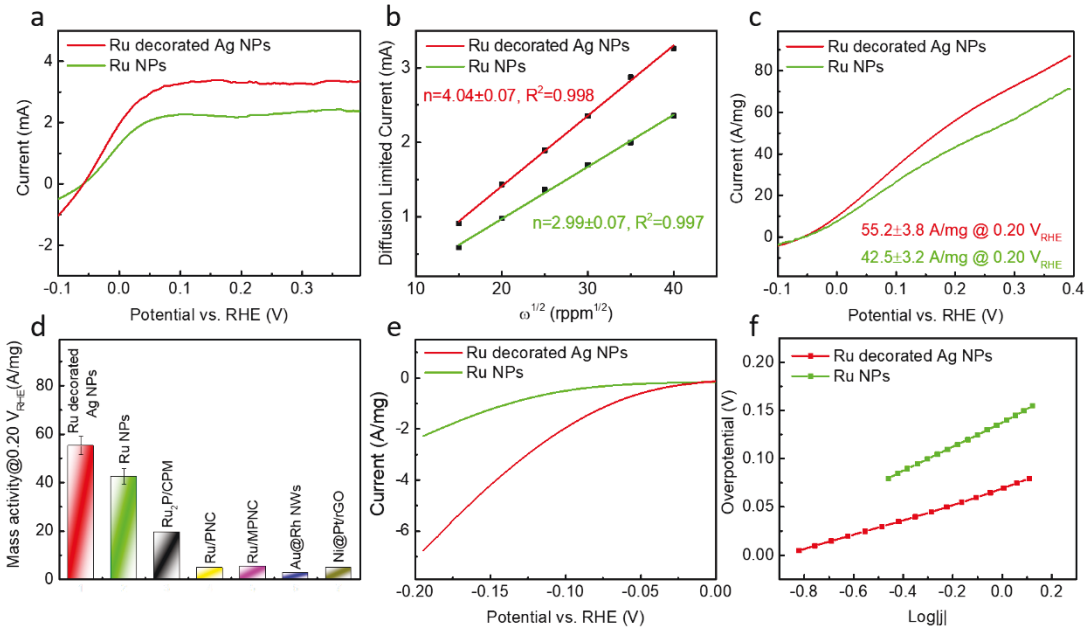

Fig. 2 Electrochemical study on single electrode. (a) LSV curves of Ru@Ag NPs and ultrasmall Ru NPs in 1.0 M KOH + 5.0 mM N_2H_4 electrolyte at rotation rate of 1600 rppm. (b) Linear fitting of the diffusion limited current at different rotation rate. (c) Mass loading normalized LSV curves of Ru@Ag NPs and ultrasmall Ru NPs in 1.0 M KOH + 0.10 M N_2H_4 electrolyte tested on gas diffusion electrode. (d) Comparison with the previously reported Ru based electrocatalyst for HzOR in terms of the MA (The average and standard deviation are reported from 3 tests) at 0.20 V vs. RHE. (e) Mass loading normalized LSV curves of Ru@Ag NPs and ultrasmall Ru NPs in 1.0 M KOH electrolyte at rotation rate of 1600 rppm. (f) Tafel slopes of Ru@Ag NPs and ultrasmall Ru NPs as HER electrocatalysts.

The HzOR performance was first evaluated on RDE using 5.0 mM hydrazine in 1.0 M KOH electrolyte with linear sweep voltammetry (LSV). The Ru@Ag NPs present a 10-mV lower halfwave potential compared with Ru NPs and a higher diffusion limited current than the Ru NPs (~3.3 mA for Ru@Ag NPs vs ~2.4 mA for Ru NPs) (Fig. 2a).The linear fitting according to the Levich equation (Eq. 3) between the diffusion limited currents and the square root of the corresponding rotation rates yields an electron transfer number of 4.04±0.07 for Ru@Ag NPs and 2.99±0.07 for ultrasmall Ru NPs, indicating the selective electrooxidation of hydrazine into N_2 on Ru@Ag NPs presenting Ag-Ru interfaces while the ultrasmall Ru NPs are unable to achieve that (Fig. 2b and Fig. S3, ESI†).

$$\mathbf{I_{DL} = 0.201nFAD_R^{2/3}\nu^{-1/6}C\omega^{1/2}} \quad (3)$$

This result is in good agreement with the previous literature, where Ru catalyst could facilitate N-N cleavage, leading to ammonia as potential byproducts and a lowered electron transfer number[12, 15, 25, 26].

To move one step closer to real world application scenarios, the HzOR performances were also tested on the gas diffusion electrode (Fig. 2c). Importantly, the Ru@Ag NPs demonstrate a high mass activity of 55.2±3.8 A/mg at 0.20 V vs. RHE, which is 1.3-fold higher than Ru NPs (42.5±3.2 A/mg) and also surpasses many of the previously reported noble metal based electrocatalysts, including Ru_2P/N, P dual-doped carbon porous microsheets (Ru_2P/CPM)[27], Ru/mesoporous N-doped carbon (Ru/MPNC)[28], Ru/porous N-doped carbon (Ru/PNC)[29], Au@Rh core-shell nanowires (Au@Rh NWs)[30], Ni@Pt/RGO electrocatalysts (Fig. 2d)[31]. In addition, the Ru@Ag NPs also demonstrate better long-term performance than the ultrasmall Ru NPs, showing a higher current density at 0.20 V vs. RHE after one-hour of chronoamperometry (CA) test (Fig. S4, ESI†).

The performance for the cathode HER was also tested and the Ru@Ag NPs exhibit a mass activity of 1.00±0.02 A/mg at -70 mV vs. RHE, which is 3.6-fold-higher than that of the ultrasmall Ru NPs (0.28±0.03 A/mg at -70 mV vs. RHE) (Fig. 2e). In addition, the Tafel slope of Ru@Ag NPs (77.4±1.4 mV/dec) is also much lower than that of the Ru NPs (121±4 mV/dec) (Fig. 2f), suggesting more favourable kinetics. CP studies also demonstrate improved long-term performance during 10-hour testing at current density of 10.0 mA/cm^2 (Fig. S5, ESI†).

Hydrazine assisted water electrolysis

We have further employed Ru@Ag NPs as both the anodic HzOR and cathodic HER electrocatalysts loaded on carbon paper in an MEA to construct a full electrolyser (noted Ru@Ag NPs||Ru@Ag NPs). Significantly, at a low mass loading of 0.20 mg_{Ru}/cm^2, the Ru@Ag NPs||Ru@Ag NPs electrolyser delivers a high current density of 100 mA/cm^2 at an ultralow voltage of 16 mV and an ultrahigh geometric current density of 983±30 mA/cm^2 at 0.45 V (Fig. 3a), thanks to the highly effective electrocatalysts and low serial resistance (Rs) in MEA (Rs=0.356±0.006 Ohm in Fig. 3b). Our studies show that Ru@Ag NPs considerably outperform the electrolysers employing ultrasmall Ru NPs (673±17 mA/cm^2 @0.45 V) and commercial Ru/C catalysts (378±15 mA/cm^2 @0.45 V). The EIS analysis also demonstrates the lowest charge transfer resistance for the Ru@Ag NPs||Ru@Ag NPs electrolyser (Fig. 3b), consistent with the optimized catalytic performance. In contrast, the traditional water electrolyser without hydrazine requires a much higher voltage (e.g., 1.75 V higher for the Ru@Ag NPs||Ru@Ag NPs electrolyser without the introduction of hydrazine in Fig. 3c). The long-term performances were also studied via CP at 100 mA/cm^2 for 10 h and the Ru@Ag NPs||Ru@Ag NPs electrolyser also requires considerably lower voltage to maintain

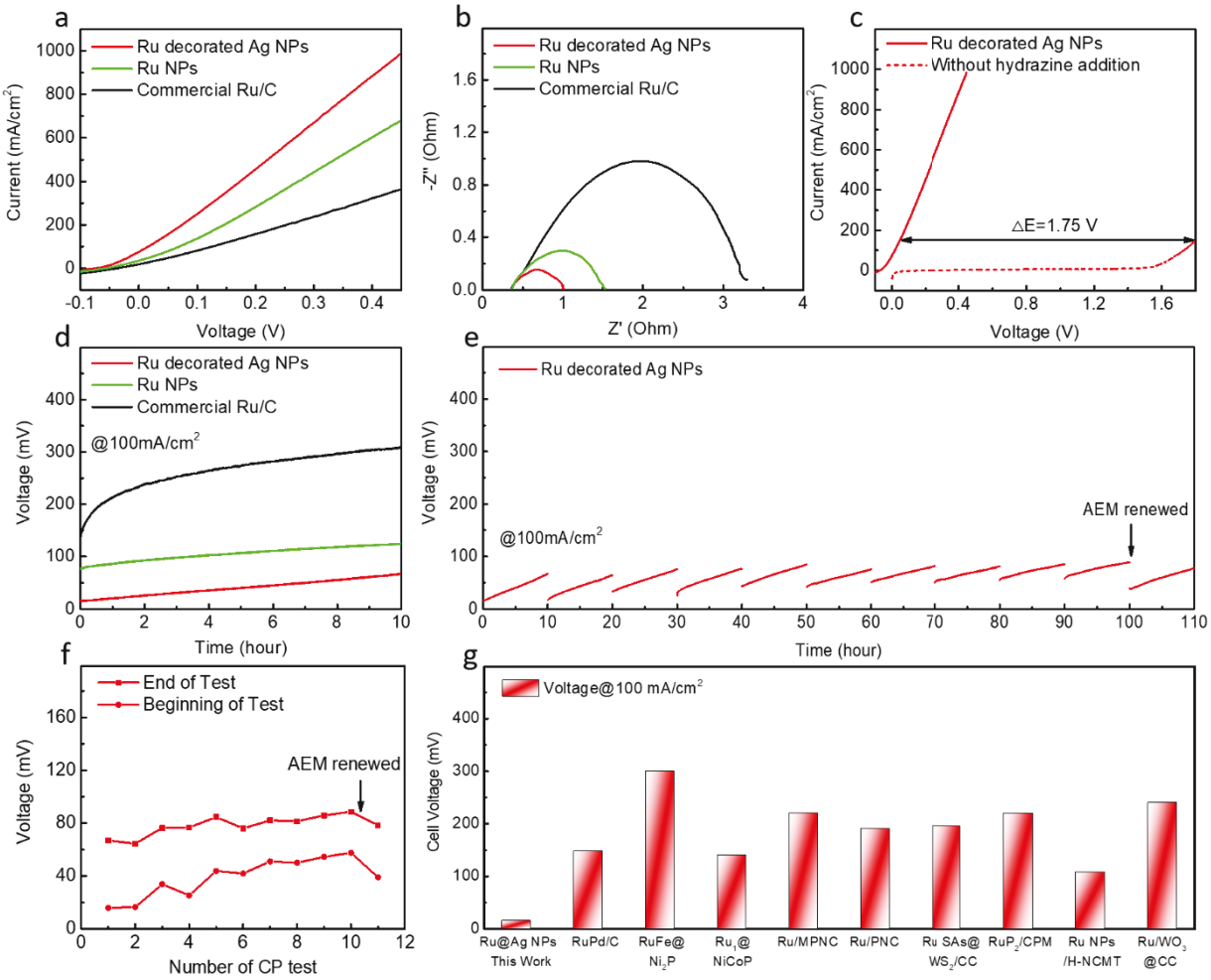

Fig. 3 Hydrazine assisted water electrolysis performance test (Loading: 0.2 mg_{Ru}/cm^2). (a) Polarization curves of the electrolyser with Ru@Ag NPs||Ru@Ag NPs, ultrasmall Ru NPs||ultrasmall Ru and commercial Ru/C||commercial Ru/C electrolysers in the 1.0 M KOH + 1.0 M N_2H_4 electrolyte. (b) EIS tests of the electrolysers. (c) Comparisons of the polarization curves of Ru@Ag NPs||Ru@Ag NPs in the 1.0 M KOH + 1.0 M N_2H_4 and 1.0 M KOH electrolyte. (d) CP tests of the electrolysers at current density of 100 mA/cm2. (e) Repeated CP tests of the Ru@Ag NPs||Ru@Ag NPs electrolyser for 110 hours. (f) Cell voltage at the beginning and the end of each 10-hour CP test. (g) Performance comparison with the previously reported state-of-the-art Ru-based hydrazine assisted water electrolysers.

100 mA/cm^2 throughout the testing period (Fig. 3d). In addition, although there is around 30-50 mV voltage increase after each CP test, refreshing the electrolyte and replacing the AEM can recover the performance of the electrolyser (Fig. 3e). Overall, there are only 23-mV increase by comparing the beginning of 1st and 11th 10-hour test (Fig. 3f) and only ~5% performance decay after 10 rounds of 10 h CP test (Fig. S6, ESI†).

The quantification of hydrogen gas showed a Faradaic efficiency of 95.9±1.4%, which is consistent with the theoretical value (Fig. S7, ESI†) within the instrumental error. Our NMR analysis revealed that there is little ammonia byproduct present in the reaction solution after 10 h of CP test at 100 mA/cm^2, (with a FE of only 1.1±0.2% for ammonia byproduct, see Fig. S8, ESI†), confirming the nearly 100% FE selective electrooxidation of hydrazine into N_2. This byproduct analysis agrees well with the electron transfer number determined from the RDE studies. In sharp contrast, the reaction with the Ru NPs catalysts demonstrates much more evident ammonia byproduct with a FE of 14.2±1.6% for ammonia byproducts. These analyses are generally consistent with electron transfer number determined from our RDE studies. Significantly, the performance of our electrolyser employing the Ru@Ag NPs (16 mV@100 mA/cm^2, 983±30 mA/cm^2 @0.45 V without any IR compensation) is the most optimized so far to our best knowledge. For example, at least 0.1 V cell voltage is lowered to reach a current density of 100 mA/cm^2 compared with the previously reported state-of-the-art Ru-based hydrazine assisted water electrolysers employing RhPd/C[32], Ru, Fe dual doped Ni_2P (RuFe@Ni_2P)[33], Ru single atoms on NiCoP nanowire (Ru_1@NiCoP)[34], Ru/MPNC[28], Ru/PNC[29], Ru single atoms@WS_2/conductive carbon (Ru SAs@WS_2/CC)[35], RuP_2/CPM[27], Ru nanoparticles supported on the hollow N-doped carbon microtube (Ru NPs/HNCMT)[36], Ru single atoms/WO_3@carbon cloth (Ru/WO_3@CC)[37] (Fig. 3g), a more detailed comparison is listed in Table S1, ESI†. We have further characterized the anode and cathode electrocatalysts after CP test. The TEM and HRTEM studies show that the morphology and crystallinity of the NPs are generally retained (Fig. S9 and 10, ESI†). XRD reveals that the minor AgCl of the as-prepared Ru@Ag NPs completely disappears after the CP test,

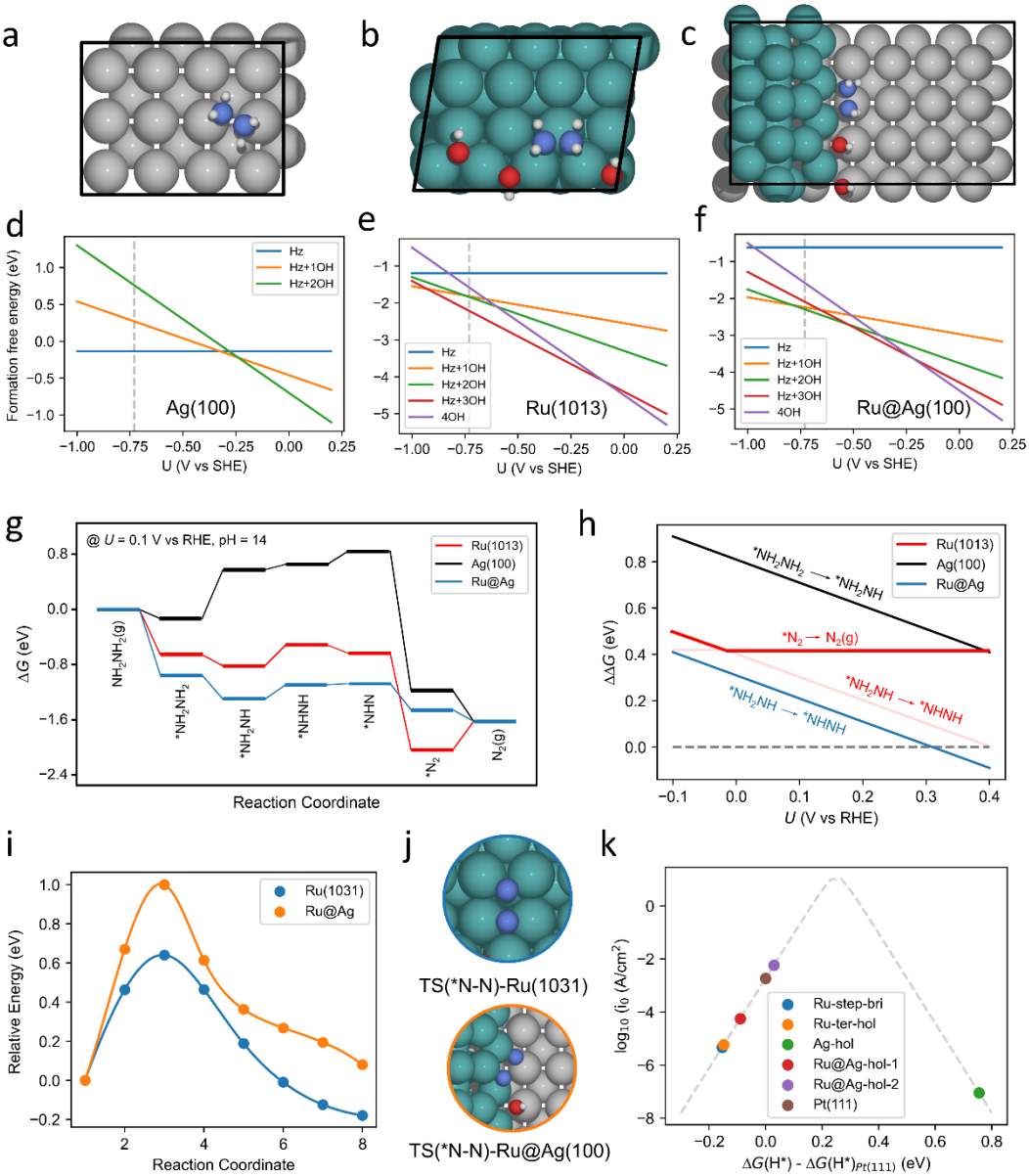

Fig. 4 DFT calculations. Three representative models in this study, (a) Ag (100) with one $*NH_2NH_2$ (b) Ru (1013) with one $*NH_2NH_2$ and three *OH species (c) Ru@Ag (100) interface model with one $*NH_2NH_2$ and three *OH species. Stability diagram for (d) Ag (100) (e) Ru (1031) and (f) Ru@Ag (100) as a function of *OH coverage. (g) Reaction energy profile for hydrazine oxidation on our three models at 0.1 V vs RHE and pH 14. (h) Comparison of potential-determining steps as the function of electrode potential for the three catalyst models. $*N_2$ to N_2 (g) is a chemical step which is potential-independent, which accounts for its representation as a horizontal line in the graph. (i) Reaction barriers for N-N bond cleavage on Ru (1031) and on the Ru@Ag (100) interface. (j) The structure of the transition state for N-N bond cleavage on Ru (1031) and on the Ru@Ag (100) interface. (k) Simulated exchange current i_0 for HER as a function of *H adsorption free energy for the locally stable adsorption sites on the three models.

indicating the reduction of AgCl to Ag under working conditions (Fig. S11, ESI†). EDX studies confirm the ultrasmall Ru NPs remain decorated on the Ag NPs surface (Fig. S12 and 13, ESI†). XPS study illustrates the binding energy and the elemental ratio of the electrocatalysts surface remain similar (Ru:Ag=1.00:1.20 for cathode electrocatalysts and 1.00:1.12 for anode electrocatalysts, Fig. S14, ESI†). The Inductively coupled plasma mass spectrometry (ICP-MS) also indicates negligible electrocatalyst dissolution after CP test (<<0.1% of the initial loading). These characterizations confirm the stability of the electrocatalysts under long-term of operation.

We also tentatively analysed the techno-economic aspects. Beyond the capital equipment cost, electricity contributes a major fraction of the total hydrogen production cost. Considering hydrazine assisted water electrolysis can be achieved at a much lower potential, ~1.75 V lower than that needed for direct water electrolysis, this could substantially reduce the required electricity for hydrogen production (~46.9 kWh less electricity per kg H_2), leading to significant cost reduction ($7.13/kg$H_2$ considering industrial electricity cost is $0.152/kWh in California). The hydrazine is from industrial wastewater so that the cost of hydrazine in this case is negligible. Additionally, direct conversion of waste hydrazine into

hydrogen could also help mitigate relevant environmental issues and thus bring additional societal benefit.

Theoretical computation

DFT calculations were employed to gain insights into the reaction mechanism underlying hydrazine-assisted water electrolysis. For the analysis of HzOR and HER, three representative catalyst models were constructed. The selection of the Ag (100) surface was based on our HERTEM characterization. Considering that the size of Ru NPs (~2.5 nm) is slightly above 2 nm, it is expected that these nanoparticles predominantly consist of edge and corner sites, as well as B5 sites, which play a crucial role in ammonia synthesis[38]. Therefore, the (1013) surface was chosen as a model since it encompasses a diverse range of local surface environments, such as steps, square sites, triangle sites, and B5 sites (Fig. S15, ESI†). Additionally, an Ag (100) supported Ru rod model was constructed to mimic the Ru-Ag interface.

Determining the nature of the active phase during the reaction is crucial for comprehending the reaction mechanism. In the case of the oxidation process, co-adsorption of *OH is of utmost importance (adsorbed species are indicated with an asterisk). To investigate the OH coverage, calculations were conducted with and without the presence of $*NH_2NH_2$. Based on the surface stability diagram, it becomes evident that under the reaction conditions, specifically at -0.73 V vs SHE, the Ag (100) surface remains clean and does not exhibit any *OH adsorption (Fig. 4a, d). In addition, the adsorption of $*NH_2NH_2$ is slightly exergonic. For the Ru (1031) surface, only adsorption of OH on top of the step edge was considered for simplicity, since this is the strongest binding site. Within this step edge, it was observed that the most stable configuration, within the chosen potential range, involved the adsorption of $*NH_2NH_2$ along with 3*OH species for the selected super cell including 4 Ru atoms along the step (Fig. 4d, e). In the case of the Ru@Ag (100) interface, the adsorbate coverage was found to depend on the electrode potential. Starting from -1 V vs SHE, as the potential becomes more positive, the interface initially exhibits $*NH_2NH_2$ and 1*OH adsorption, followed by $*NH_2NH_2$ and 2*OH adsorption, and eventually * NH_2NH_2 and 3*OH, for the chosen super cell containing 4 Ru interface atoms. When the potential is more positive than -0.22 V vs SHE, *OH adsorption becomes more favorable than * NH_2NH_2 adsorption, resulting in a full coverage of 4 *OH on the interface, and no $*NH_2NH_2$ adsorbed. At -0.73V vs SHE, the interface is characterized by $*NH_2NH_2$ with 2*OH adsorption (Fig. 4c, f), and this configuration was selected to evaluate the activity of the HzOR.

At a reaction potential of 0.1 V vs RHE and pH = 14 (equivalent to -0.73 V vs SHE), we investigated the mechanism of HzOR on the three representative models (Fig. 4g). Our findings indicate that $*NH_2NH_2$ exhibits a strong binding affinity at the Ru@Ag (100) interface, followed by the Ru (1031) steps and the Ag (100) terrace sites, in descending order of binding strength. As the reaction progresses, it is observed that each dehydrogenation elementary step from $*NH_2NH_2$ to *NHN is endergonic on the Ag (100) surface. This results in a significant energy span associated with these dehydrogenation steps on Ag (100). Conversely, for the Ru (1013) surface, the adsorption strength of intermediates is moderate except for $*N_2$ adsorption. The presence of the B5 site on Ru (1013) provides a favorable binding space for $*N_2$, thus facilitating its adsorption. Consequently, $*N_2$ desorption becomes challenging for the Ru (1013) surface. Regarding the Ru@Ag (100) interface, the dehydrogenation steps of $*NH_2NH$ to $*NH_2N$ exhibit a slight endergonic nature, with a reaction free energy of approximately 0.22 eV. However, the remaining elementary steps are all exergonic. Based on the thermodynamic energy profile, with only one modest endergonic step, we can conclude that the Ru@Ag (100) interface displays the highest activity for hydrazine oxidation under the specified conditions.

We also explored the potential-determining step (PDS) of the reaction pathway as a function of the electrode potential (Fig. 4h). For Ag (100), we observed that the potential-determining step (PDS) in a wide range of potential is the dehydrogenation of $*NH_2NH_2$ to $*NH_2NH$, and it shows a high reaction energy. This indicates that the Ag (100) surface cannot serve as the active site for HzOR. As for Ru (1013), the PDS switches from the dehydrogenation of $*NH_2NH$ to $*N_2$ desorption. When the potential becomes more negative than -0.02 V vs RHE, dehydrogenation of $*NH_2NH$ to *NHNH limits the overall activity, while $*N_2$ desorption becomes increasingly challenging when the potential is more positive than this threshold value. On the Ru@Ag (100) interface, in contrast, $*NH_2NH$ to *NHNH is always the PDS and always shows the smallest positive reaction energy compared to Ru (1013) and Ag (100), which implies that within the considered operating potential range, the Ru@Ag (100) interface is consistently more favorable for HzOR, yielding the highest output potential.

The feasibility of the N-N bond cleavage plays a crucial role in determining the selectivity of HzOR. There are numerous possibilities for N-N bond cleavage along the reaction pathway, and here breaking the N-N bond of $*N_2$ was chosen as the model to investigate the structure sensitivity of this elementary process. Our results show that on the B5 site of Ru (1013), the N-N bond cleavage is endergonic and occurs more readily compared to the Ru@Ag (100) interface (Fig. 4i). This can be attributed to the presence of B5 sites, which provide a step-bridge site and a hollow site to stabilize the 2*N species. which has also been observed in the ammonia synthesis[38] (Fig. 4j). The high reaction barrier for N-N bond cleavage on the interface (1 eV) suggests that the interface could inhibit N-N bond breaking along the reaction pathway at room temperature, thereby improving the selectivity for N_2 production.

In our experimental studies, we have demonstrated that Ru-decorated Ag NPs exhibit superior HER activity compared to pure Ru NPs compared with ultrasmall Ru NPs. DFT models was also used to explore the origin of this enhanced HER activity. All potential adsorption sites for hydrogen on our three model surfaces were systematically explored to evaluate the HER activity. Our investigations revealed that H adsorption on the Ag (100) surface is extremely weak, whereas on the Ru (1013) surface, H adsorption is significantly stronger (Fig. 4k). Interestingly, the interface between Ag and Ru exhibits moderate H adsorption, suggesting that, in principle, the interface should be more active for HER. We also conducted simulations to model the current density of HER[39] and found that both too weak and too strong H binding can limit the HER ability on Ag and Ru surfaces, respectively. Remarkably, the interface hollow sites, which contain both Ag and Ru components, exhibit a closer proximity to the peak of the activity volcano and thus promise

an even higher activity than Pt (111), a well-known catalyst for HER. Importantly, this is also proved experimentally, in which Ru@Ag NPs show mass activity of 1.00±0.02 A/mg at -70 mV vs. RHE in comparison with 0.58±0.03 A/mg for Pt/C and 0.28±0.03 A/mg for Ru NPs (Fig. S16, ESI†), which generally agrees with the result from previous literature[40]. Consequently, the observed higher HER activity can be attributed to the regulation of H adsorption strength at the Ag-Ru interface.

Conclusions

In summary, we have designed and synthesized Ru decorated Ag NPs via a facile one-pot polyol method, as a bifunctional electrocatalyst with outstanding performance for HzOR and improved activity for HER in alkaline condition, enabling a hydrazine assisted water electrolyser with record-high performance (16 mV@100 mA/cm^2, 983±30 mA/cm^2 @0.45 V) without any IR compensation as well as excellent long-term performance, which far outperforms all the previously reported hydrazine assisted water electrolysers. DFT study reveals that the Ag-Ru interface, compared to Ag or Ru surfaces, shows the most favourable energy profile for HzOR with facilitated N_2 desorption while inhibiting the N-N bond cleavage, leading to the highest HzOR activity and selective electrooxidation into N_2. Meanwhile, the HER performance is enhanced at the Ag-Ru interface due to a near-optimal hydrogen adsorption strength. This work sheds lights on interface engineering of bifunctional electrocatalysts for hydrazine assisted water electrolysis, opening a pathway to low voltage hydrogen production along with industrial waste water treatment.

Author Contributions

X.F. and X.D. conceived and designed this research. X.F. synthesized the electrocatalysts, studied the electrocatalytic performance. X.F., A.Z., Z.J. and S.W. performed the characterization. X.F. carried out the hydrazine assisted water electrolysis test with the help from X. Z. and J. C., D.C. and P.S. conceived and conducted the theoretical study. All authors contributed to the analysis and interpretation of the results. X.F., D.C., P.S., Y.H. and X.D wrote the manuscript.

Conflicts of interest

There are no conflicts to declare.

Acknowledgements

X.D. and Y.H. acknowledge the gracious support by NewHydrogen, Inc. D.C. and P.S. acknowledge support from the National Science Foundation award 2103116. D. C. used the HOFFMAN2 cluster at the UCLA Institute for Digital Research and Education (IDRE). We also acknowledge the help with characterizations from Zahra Zare and Professor Brent Melot from USC department of chemistry.

References

1. H. Liu, Y. Liu, M. Li, X. Liu and J. Luo, *Materials Today Advances*, 2020, **7**, 100083.
2. J. K. Niemeier and D. P. Kjell, *Org. Process Res. Dev.*, 2013, **17**, 1580-1590.
3. T. Sakamoto, A. Serov, T. Masuda, M. Kamakura, K. Yoshimoto, T. Omata, H. Kishi, S. Yamaguchi, A. Hori, Y. Horiuchi, T. Terada, K. Artyushkova, P. Atanassov and H. Tanaka, *J. Power Sources*, 2018, **375**, 291-299.
4. Who, Lyon, FRANCE, 2006.
5. H. Liu, Y. Liu, M. Li, X. Liu and J. Luo, *Mater. Today Adv.*, 2020, **7**, 100083.
6. S.-W. Kim, S.-Y. Park, C.-H. Roh, J.-H. Shim and S.-B. Kim, *Chemical Papers*, 2022, **76**, 6517-6522.
7. H. Y. Wang, M. L. Sun, J. T. Ren and Z. Y. Yuan, *Adv. Energy Mater.*, 2023, **13**, 2203568.
8. S. Y. Kang, J. E. Park, G. Y. Jang, O.-H. Kim, O. J. Kwon, Y.-H. Cho and Y.-E. Sung, *Int. J. Hydrogen Energy*, 2022, **47**, 9115-9126.
9. J. Parrondo, C. G. Arges, M. Niedzwiecki, E. B. Anderson, K. E. Ayers and V. Ramani, *RSC Adv.*, 2014, **4**, 9875-9879.
10. K. Chau, A. Djire and F. Khan, *Int. J. Hydrogen Energy*, 2022, **47**, 13990-14007.
11. S. A. Grigoriev, P. Millet, S. V. Korobtsev, V. I. Porembskiy, M. Pepic, C. Etievant, C. Puyenchet and V. N. Fateev, *Int. J. Hydrogen Energy*, 2009, **34**, 5986-5991.
12. D. A. Finkelstein, R. Imbeault, S. Garbarino, L. Roue and D. Guay, *J. Phys. Chem. C*, 2016, **120**, 4717-4738.
13. J. A. Herron, P. Ferrin and M. Mavrikakis, *J. Phys. Chem. C*, 2015, **119**, 14692-14701.
14. A. O. Elnabawy, J. A. Herron, S. Karraker and M. Mavrikakis, *J. Catal.*, 2021, **397**, 137-147.
15. J. Zhang, Y. X. Wang, C. J. Yang, S. Chen, Z. J. Li, Y. Cheng, H. N. Wang, Y. Xiang, S. F. Lu and S. Y. Wang, *Nano Res.*, 2021, **14**, 4650–4657.
16. K. Asazawa, T. Sakamoto, S. Yamaguchi, K. Yamada, H. Fujikawa, H. Tanaka and K. Oguro, *J. Electrochem. Soc.*, 2009, **156**, B509-B512.
17. Y. H. Liu, Q. L. Wang, J. C. Zhang, J. Ding, Y. Q. Cheng, T. Wang, J. Li, F. X. Hu, H. B. Yang and B. Liu, *Adv. Energy Mater.*, 2022, **12**, 2200928.
18. W. J. Luo, Y. J. Wang and C. W. Cheng, *Mater. Today Phys.*, 2020, **15**, 100274.
19. S. Zhang, J. Li and E. R. Wang, *Chemelectrochem*, 2020, **7**, 4526-4534.
20. H. E. Hoster, *MRS Online Proceedings Library*, 2012, **1388**, 10.
21. Y. J. Yang, Y. H. Yu, J. Li, Q. R. Chen, Y. L. Du, P. Rao, R. S. Li, C. M. Jia, Z. Y. Kang, P. L. Deng, Y. J. Shen and X. L. Tian, *Nano-Micro Letters*, 2021, **13**, 160.
22. C. H. Chen, D. Wu, Z. Li, R. Zhang, C. G. Kuai, X. R. Zhao, C. K. Dong, S. Z. Qiao, H. Liu and X. W. Du, *Adv. Energy Mater.*, 2019, **9**, 1803913.
23. N. Maity, A. Sahoo, R. Boddhula, S. Chatterjee, S. Patra and B. B. Panda, *Dalton Trans.*, 2020, **49**, 11019-11026.
24. Z. Che, X. Lu, B. Cai, X. Xu, J. Bao and Y. Liu, *Nano Res.*, 2022, **15**, 1269-1275.
25. K. Yamada, K. Yasuda, H. Tanaka, Y. Miyazaki and T. Kobayashi, *J. Power Sources*, 2003, **122**, 132-137.

26. X. Y. Fu, D. F. Cheng, C. Z. Wan, S. Kumari, H. T. Zhang, A. Zhang, H. Huyan, J. X. Zhou, H. Y. Ren, S. B. Wang, Z. P. Zhao, X. Zhao, J. Chen, X. Q. Pan, P. Sautet, Y. Huang and X. F. Duan, *Adv. Mater.*, 2023, **35**, 2301533.
27. Y. P. Li, J. H. Zhang, Y. Liu, Q. Z. Qian, Z. Y. Li, Y. Zhu and G. Q. Zhang, *Sci. Adv.*, 2020, **6**, abb4197.
28. J. S. Wang, X. Y. Guan, H. B. Li, S. Y. Zeng, R. Li, Q. X. Yao, H. Y. Chen, Y. Zheng and K. G. Qu, *Nano Energy*, 2022, **100**, 107467.
29. X. Y. Guan, Q. N. Wu, H. B. Li, S. Y. Zeng, Q. X. Yao, R. Li, H. Y. Chen, Y. Zheng and K. G. Qu, *Appl. Catal. B-Environ.*, 2023, **323**, 122145.
30. Q. Xue, H. Huang, J. Y. Zhu, Y. Zhao, F. M. Li, P. Chen and Y. Chen, *Appl. Catal. B-Environ.*, 2020, **278**, 10.
31. M. G. Hosseini, R. Mahmoodi and M. Abdolmaleki, *New J. Chem.*, 2018, **42**, 12222-12233.
32. S. Zhao, Y. Zhang, H. Li, S. Zeng, R. Li, Q. Yao, H. Chen, Y. Zheng and K. Qu, *J. Mater. Chem. A*, 2023, **11**, 13783-13792.
33. X. Zhai, Q. Yu, J. Chi, X. Wang, B. Li, B. Yang, Z. Li, J. Lai and L. Wang, *Nano Energy*, 2023, **105**, 108008.
34. Y. Hu, T. Chao, Y. Li, P. Liu, T. Zhao, G. Yu, C. Chen, X. Liang, H. Jin and S. Niu, *Angew. Chem.*, 2023, **135**, e202308800.
35. J. C. Li, Y. Li, J. A. Wang, C. Zhang, H. J. Ma, C. H. Zhu, D. D. Fan, Z. Q. Guo, M. Xu, Y. Y. Wang and H. X. Ma, *Adv. Funct. Mater.*, 2022, **32**, 2109439.
36. W. Wang, Q. Qian, Y. Li, Y. Zhu, Y. Feng, M. Cheng, H. Zhang, Y. Zhang and G. Zhang, *ACS Applied Materials Interfaces*, 2023, **15**, 26852–26862.
37. J. Li, C. Zhang, C. Zhang, H. Ma, Y. Yang, Z. Guo, Y. Wang and H. Ma, *Chem. Eng. J.*, 2022, **430**, 132953.
38. K. Honkala, A. Hellman, I. N. Remediakis, A. Logadottir, A. Carlsson, S. Dahl, C. H. Christensen and J. K. Norskov, *Science*, 2005, **307**, 555-558.
39. J. K. Nørskov, T. Bligaard, A. Logadottir, J. R. Kitchin, J. G. Chen, S. Pandelov and U. Stimming, *Journal of The Electrochemical Society*, 2005, **152**.
40. Y. Zheng, Y. Jiao, Y. Zhu, L. H. Li, Y. Han, Y. Chen, M. Jaroniec and S.-Z. Qiao, *J. Am. Chem. Soc.*, 2016, **138**, 16174-16181.

